JCTC Journal of Chemical Theory and Computation

pubs.acs.org/JCTC Article

Alchemical Free Energy and Hamiltonian Replica Exchange Molecular Dynamics to Compute Hydrofluorocarbon Isotherms in Imidazolium-Based Ionic Liquids

Ning Wang,[†] Ryan S. DeFever,[†] and Edward J. Maginn*

Cite This: J. Chem. Theory Comput. 2023, 19, 3324−3335 Read Online

ACCESS | Metrics & More | Article Recommendations | Supporting Information

ABSTRACT: Ionic liquids (ILs) have shown promise for applications that leverage differential gas solubility in an IL solvent, e.g., gas separations. Although most available literature provides Henry's law constants, the ability to efficiently estimate full isotherms is important for engineering design calculations. Molecular simulation can be used as a tool to predict full isotherms of gas in ILs. However, particle insertions or deletions in a charge-dense IL medium and the sluggish conformational dynamics of ILs present two sampling challenges for these systems. We therefore devised a method that uses Hamiltonian replica exchange (HREX) molecular dynamics (MD) combined with alchemical free energy calculations to compute full solubility isotherms of two different hydrofluorocarbons (HFCs) in imidazolium-based IL binary mixtures. This workflow is significantly faster than the Gibbs ensemble Monte Carlo (GEMC) simulations which fail to deal with the slow conformational relaxation caused by the sluggish dynamics of ILs. Multiple free energy estimators, including thermodynamic integration, free energy perturbation, and multistate Bennett acceptance ratio method, provided consistent results. Overall, the simulated Henry's law constant, isotherm curvature, and solubility trends match experimental results reasonably well. We close by calculating the full solubility isotherms of two HFCs in IL mixtures that have not been reported in the literature, demonstrating the potential of this method to be used for solubility prediction and setting the stage for future computational screening studies that search for the "best" IL to separate azeotropic HFC mixtures.

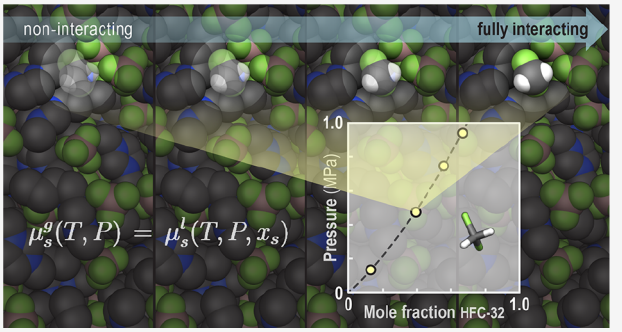

INTRODUCTION

Ionic liquids (ILs) are formally defined as molten salts with melting temperatures below 373 K,[1] although many ILs have melting points below room temperature. They have come under intense research for applications in a number of areas including separations, catalysis, bioprocessing, pharmaceutical production, electrochemistry, and metal finishing. There are over 17 000 patents on ILs and at least 50 pilot- or full-scale commercial processes that use ILs.[2] Many ILs have vanishingly low vapor pressures and readily dissolve gases, which has made them especially attractive for gas separation applications. A recent review[3] reported that there were over 200 publications from 2012 to 2017 on the "solubility of gases in ionic liquids", and a review by Lei et al. in 2014 covers the solubilities for several gases including water, hydrocarbons, and hydrofluorocarbons (HFCs) in a variety of ILs.[4]

Much of the experimental solubility data in the literature are reported as Henry's law constants, which are only relevant at low pressures and dilute gas concentrations. For many applications, full solubility isotherms over a range of pressures and compositions are needed.[3] The full isotherms can be fit to equations of state and then used for engineering calculations.[5]

It is also possible to compute Henry's law constants and full isotherms of gases and small molecules in ILs using molecular simulation. Lynden-Bell et al. first calculated the excess chemical potentials (related to Henry's law constants) of water, methanol, dimethyl ether, acetone, and propane in dimethylimidazolium chloride at 400 K using molecular dynamics (MD) simulations along with thermodynamic integration.[6] Other researchers employed the test particle (Widom) insertion method to estimate Henry's constants of CO_2 in 1-*n*-butyl-3-methylimidazolium hexafluorophosphate ($[C_4C_1im][PF_6]$) via Monte Carlo (MC) simulation.[7] However, the predicted solubilities were 2−2.5 times below experimental values,[7] probably due to the accuracy of the united atom force field employed and the systematic errors, convergence, and finite-size effects associated with the Widom insertion method. These authors later employed expanded

Received: February 20, 2023
Published: May 17, 2023

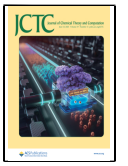

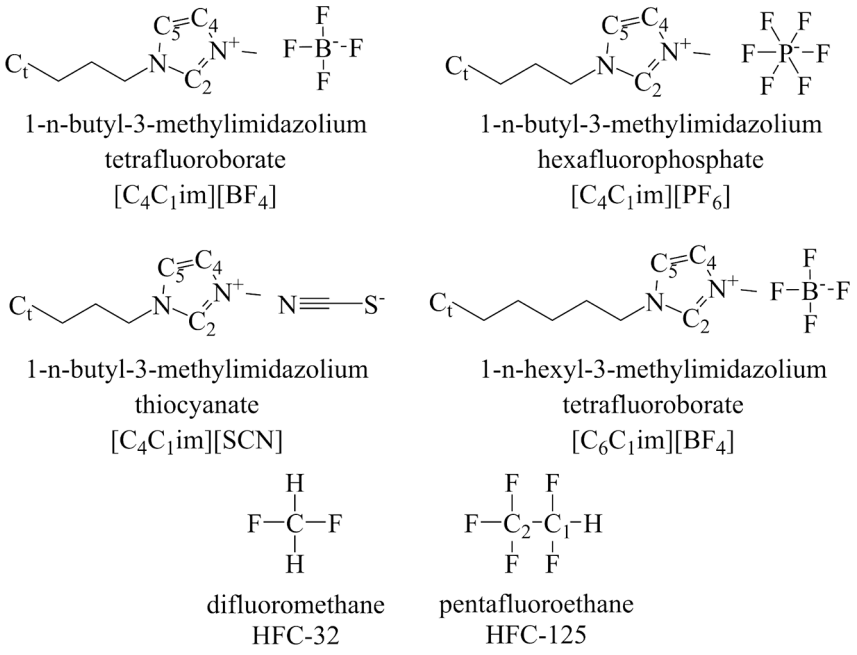

Figure 1. Chemical structures and names of studied HFCs and ILs.

ensemble methods and showed that this improved sampling and accuracy relative to the standard Widom insertion approach.[8] Liu et al. systematically studied Henry's constants of eight common polar and nonpolar gases in 1-ethyl-3-methylimidazolium bis(trifluoromethylsulfonyl)imide ($[C_2C_1im][Tf_2N]$) using MD simulations along with Bennett acceptance ratio (BAR) analysis to obtain better statistics.[9] Both the solubility trend and temperature dependence showed promising agreement with experiments. Zheng et al.[10] and Salehin et al.[11] used the same procedure to calculate Henry's constants of isobutane and 2-butene in imidazolium ILs and H_2S in cholinium-based amino acid ILs, respectively. Padua and co-workers employed an advanced polarizable ionic liquid force field along with a free energy perturbation method to compute Henry's law constants of fluorinated refrigerant gases in ILs.[12] They found good agreement with experiment, but the expense of the polarizable model meant they could only simulate high temperatures due to the sluggish dynamics of the IL.

The first example of simulations being used to compute entire isotherms was from Maurer et al.,[13] who applied Gibbs ensemble Monte Carlo (GEMC) simulations within the isothermal−isobaric (*NPT*) ensemble to compute the isotherms of hydrogen, carbon monoxide, and carbon dioxide in $[C_4C_1im][PF_6]$. Although the predicted isotherm for hydrogen agreed with experiments within the uncertainty, the calculated isotherms for carbon monoxide and carbon dioxide showed large deviations from experiments.[13] A number of other authors have employed different methods to compute isotherms of gases in ILs, of which we list a few below.

Shi and Maginn employed the continuous fractional component Monte Carlo method to calculate the isotherms of carbon dioxide and water in an all-atom model of 1-*n*-hexyl-3-methylimidazolium bis(trifluoromethylsulfonyl)imide ($[C_6C_1im][Tf_2N]$) under the osmotic ensemble.[14] This advanced MC method gradually inserts or deletes molecules using an adaptive bias function, thereby overcoming some of the sampling problems associated with insertions and deletions into and out of dense media. The same authors then extended the method to both pure and mixed gas systems in $[C_6C_1im][Tf_2N]$.[15] Singh et al. used biased GEMC simulations to compute isotherms of carbon dioxide, hydrogen, and their mixtures in a series of ILs.[16] Vlugt et al. studied the absorption of ammonia in two different ILs using osmotic ensemble MC simulations.[17]

These and other studies have shown that, to obtain accurate Henry's law constants and isotherms, accurate force fields and effective sampling methods are necessary. ILs are more challenging to model than conventional molecular liquids because their viscosities tend to be higher, so their dynamics are more sluggish. Also, they do not expand much upon absorbing gases, which when combined with their strong Coulombic interactions makes it difficult to perform the types of insertions and deletions needed when employing open ensemble simulations. Thus, there are two related sampling problems that must be overcome to adequately simulate gas solubility in ILs: (1) gas insertion and deletion moves into and out of a dense charged liquid and (2) conformational relaxation of the underlying liquid structure as the composition changes.

The insertion and deletion problem can be overcome by using staged or alchemical solute transformation methods, where we slowly turn off the interactions between a solute molecule and the remainder of the system. As noted above, many of these techniques have been employed already in simulating gas solubility in ILs. In such a simulation, a nonphysical reaction coordinate λ is used to connect the fully interacting and noninteracting solute molecules. An alchemical transformation of the solute is achieved through a series of intermediate unphysical states. Because the free energy difference between the two end states is a state function, the choice of reaction coordinate will not impact the result as long as adequate sampling is achieved.

It is well-known that, even with sufficient intermediate steps, alchemical free energy methods will not converge in systems that have slow structural or reorganization dynamics as λ

https://doi.org/10.1021/acs.jctc.3c00206
J. Chem. Theory Comput. 2023, 19, 3324−3335

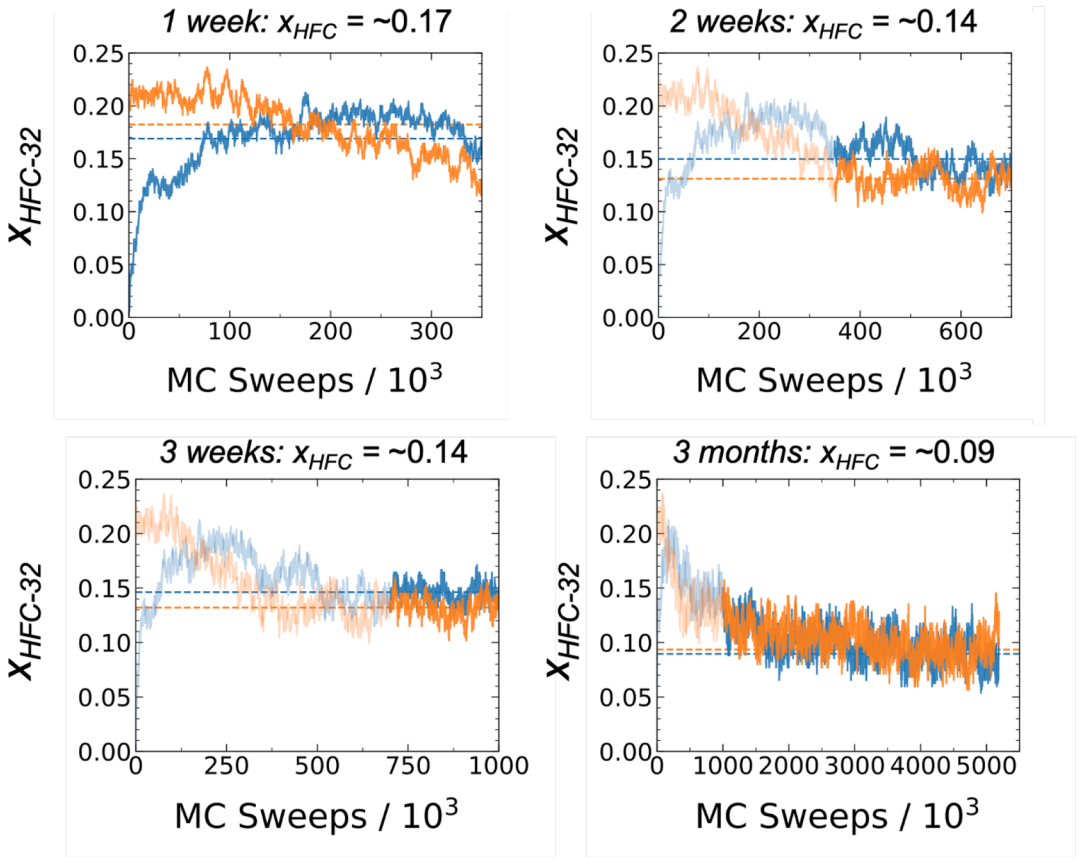

Figure 2. Convergence of two independent Gibbs ensemble MC simulations of HFC-32 in $[C_4C_1im][PF_6]$ at P = 1 bar and T = 298.15 K. While the simulations appear to converge after about 2 weeks, slow conformational changes of the IL phase result in a much longer equilibration time than expected.

changes.[18,19] This is exactly the case with ILs, which have very sluggish dynamics, especially at lower temperatures. As we will show later, the sluggish dynamics of the IL phase can give one a false impression that a system is fully equilibrated at a given composition, when in fact insufficient conformational sampling prevents the system from reaching its true equilibrium value. This is very hard to detect in a standard simulation. Thus, enhanced configurational sampling is required in addition to alchemical transformations to ensure adequate sampling.

One effective way to accelerate sampling is to use Hamiltonian replica exchange (HREX) MD simulations, in which different simulation systems (replicas) evolve according to different Hamiltonians.[20] Exchanges between the replicas are attempted at regular intervals and accepted with a criterion that maintains the correct ensemble probabilities in order to enhance sampling. Many studies of biomolecular systems have utilized HREX to enhance the configurational sampling of large molecules. Fukunishi et al.[21] developed two variants of the HREX method to study conformational sampling associated with protein folding in model systems. The method was then used for binding free energy calculations,[22] benefited the sampling of protein side chains in free energy perturbation calculations,[23] and enhanced the conformational sampling of CRT18 relative to classical MD.[24] Roitberg and co-workers[25] combined alchemical free energy calculations with HREX MD to calculate the pK_a of a model aspartic acid compound.

Here, we applied similar concepts to compute the solubilities of two HFCs, HFC-32 (CH_2F_2) and HFC-125 (CHF_2CF_3), in the ILs 1-*n*-butyl-3-methylimidazolium tetrafluoroborate ($[C_4C_1im][BF_4]$), 1-*n*-butyl-3-methylimidazolium hexafluorophosphate ($[C_4C_1im][PF_6]$), and 1-*n*-butyl-3-methylimidazolium thiocyanate ($[C_4C_1im][SCN]$). HFC-32 and HFC-125 are the two components in the commercial refrigerant HFC-410A, which is being phased out due to its high global warming potential. It has been proposed that the two HFCs (which form an azeotrope) can be separated using an IL entrainer. Solubility data in ILs are therefore important, and we compare our simulated isotherms against experimental measurements. We use multistate Bennett acceptance ratio (MBAR) analysis to obtain estimates of the Henry's law constants and complete isotherms. We also examine convergence, phase-space overlap, and consistency between multiple free energy estimators, as well as the effect of the equation of state used to estimate the chemical potentials of vapor phase HFCs. Finally, we make predictions of the full isotherms of the two HFCs in 1-*n*-hexyl-3-methylimidazolium tetrafluoroborate ($[C_6C_1im][BF_4]$), for which experimental data do not yet exist. Detailed chemical structures of the studied molecules are shown in Figure 1.

PHASE EQUILIBRIUM THEORY

The equilibrium between a gas phase HFC and a nonvolatile liquid phase IL is determined when at a given T and P the chemical potential of the HFC in the liquid phase is equal to that in the vapor phase, i.e.

$$\mu_s^l(T, P, x_s) = \mu_s^g(T, P) \quad (1)$$

where μ is the total chemical potential including the ideal and excess parts, "l" and "g" refer to the liquid and gas phase, "s"

https://doi.org/10.1021/acs.jctc.3c00206
J. Chem. Theory Comput. 2023, 19, 3324−3335

represents the solute which is the HFC molecule, and x_s is the solute concentration in the liquid phase. In standard GEMC, this condition is satisfied by the construction of different moves that allow the insertion and deletion of molecules between the vapor phase (containing only HFC) and the liquid phase (containing IL and dissolved HFC). Figure 2 shows the rate of convergence of the solubility of HFC-32 in $[C_4C_1im][PF_6]$ at P = 1 bar and T = 298.15 K using GEMC with advanced configurational biasing methods.[26] Details of GEMC simulations are documented in the Supporting Information. When two independent simulations start from no dissolved HFC-32 molecules (blue) and an initial mole fraction of HFC-32 of about 0.2 (orange), the results vary over simulation time. At around 2 weeks of simulation time (~600 000 MC sweeps), the results appear to converge to a solubility of x_{HFC} = 0.14 with some uncertainty. Allowing the simulations to run for another week (~300 000 additional sweeps), the result stays at about x_{HFC} = 0.14 but the difference between the two independent simulations grows smaller. At this point, one would be tempted to stop the simulations and report this solubility value. However, if the simulations are allowed to continue for 3 months and 5M sweeps, it is found that both simulations slowly converge to a different solubility of x_{HFC} = 0.09. This is not due to the inefficiency of the insertion or deletion of solute molecules but is instead a result of the very slow conformational relaxation of the IL phase that occurs as the HFC composition changes. Obviously, it is desirable to speed up the simulations so that results can be obtained on shorter time scales.

To do this, we recognize that it is possible to compute the two chemical potentials in eq 1 independently. In the liquid phase

$$\mu_s^l(T, P, x_s) = \Delta G_{sim}(T, P, x_s) - k_B T \ln\{V^* \Lambda^{-3} q_s(T)/N_s^l\} \quad (2)$$

where ΔG_{sim} is the excess solvation free energy of the solute in the liquid phase (relative to its ideal gas state) at a given composition, temperature, and pressure, V^* is the mean volume of the system at the state point of interest, Λ is the thermal de Broglie wavelength ($\Lambda = \sqrt{\frac{2\pi\hbar^2}{m_s k_B T}}$), N_s^l is the total number of HFC molecules in solution, and $q_s(T)$ is the single molecule ideal gas partition function.[27] Below we show that ΔG_{sim} can be calculated efficiently as a function of HFC composition using alchemical free energy methods coupled with HREX. Conformational sampling of the solute is sped up by HREX and alchemical methods, which also improve the efficiency of insertion and deletion moves.

In the vapor phase

$$\mu_s^g(T, P) = -k_B T \ln\left[\frac{q_s(T) k_B T}{\Lambda^3 P_0}\right] + k_B T \ln\left[\frac{P}{P_0}\right] + k_B T \ln(\phi) \quad (3)$$

where ϕ is the fugacity coefficient and P_0 is the reference pressure which is 1 bar. Note that $q_s(T)$ cancels when μ_s^l is set equal to μ_s^g. The fugacity coefficient ϕ can be computed relatively easily as a function of T and P through the performance of gas phase simulations. Alternatively, if the force field accurately reproduces the volumetric properties of the HFC, an accurate equation of state may be used for convenience. We chose the latter approach, since the HFC force fields we are using have been shown to be highly accurate.[28] The REFPROP package[29] was applied to obtain the data points of ϕ vs P using the Peng–Robinson (PR) equation of state model. The chemical potential of the vapor phase was then found from eq 3. Given the liquid and gas phase chemical potentials, a solubility isotherm was constructed by finding the compositions and pressures where eq 1 is satisfied.

The Henry's law constant can also be computed from the liquid phase free energy simulations using

$$H = \lim_{x\to 0}\left(\frac{P}{x}\right) = k_B T \frac{N}{V} e^{\mu^\infty/k_B T} \quad (4)$$

where N is the number of ion pairs of the IL, V is the volume, and μ^∞ is the excess chemical potential of the HFC in the IL at infinite dilution (i.e., a single HFC in the IL phase)[30] and the vapor phase is assumed to be ideal.

SIMULATION METHODS

Force Fields. Force fields for all ILs were developed from the General Amber Force Field (GAFF).[31] The HFC force fields were taken from previous work[28] where they were shown to reproduce the vapor–liquid phase equilibria of the pure HFCs very accurately. Lorentz–Berthelot combining rules[32] were used for unlike intermolecular interactions. The nonbonded 1–2 and 1–3 interactions were excluded, and the 1–4 Lennard-Jones and electrostatic interactions were scaled by factors of 0.5 and 0.8333, respectively. A detailed listing of all parameters can be found elsewhere.[33]

Simulation Details. To better overcome potential energy barriers and to enhance conformational sampling of the solute molecule, HREX MD simulations were applied using the GROMACS package[34] (version 2020.4) under the *NPT* ensemble. An alchemical method was also used to compute the free energy change associated with converting one noninteracting HFC molecule to a fully interacting molecule.

The `insert-molecules` command was used to construct the simulation box with 400 ion pairs of IL and (N_s + 1) HFC molecules, where N_s is 0, 60, 260, 500, and 800 to account for different HFC concentrations. These initial systems were then energy minimized with a steepest descent algorithm with a maximum number of steps equal to 50 000.

The equilibration and production simulations used the leapfrog stochastic dynamics integrator[35] with a 1 fs time step and a Langevin thermostat[36] with the time constant set to 1 ps. For all simulations, the temperature and pressure were 298.15 K and 1 bar, respectively. That is, we neglected the effect of the vapor phase pressure differences on the liquid phase, which is reasonable given the relatively low pressures examined here and the fact that ILs are nearly incompressible. Equilibration was performed in two stages. The first stage was a 250 ps simulation with the Berendsen barostat.[37] The second stage was a 10 ns simulation with the Parrinello–Rahman barostat.[38] The production simulations were 50 ns in length using the Parrinello–Rahman barostat. The time constant for pressure coupling was 2 ps for both barostats.

All simulations used Verlet neighbor lists as implemented in GROMACS with a tolerance of 0.0001 kJ mol^{-1} ps^{-1}. The cutoff distance for Lennard-Jones and short-range Coulombic interactions was 1.2 nm. The fast smooth particle mesh Ewald algorithm[39] was used to compute long-range Coulombic interactions, and analytical dispersion corrections to the

https://doi.org/10.1021/acs.jctc.3c00206
J. Chem. Theory Comput. 2023, 19, 3324–3335

Lennard-Jones potential were applied to both energy and pressure.

$\Delta G_{sim}(T, P, x_s)$ was computed by connecting a beginning state, A, in which there are $N_s + 1$ fully interacting HFC molecules and an ending state, B, in which one of the HFC molecules has its intermolecular interactions with the system turned off, resulting in only N_s fully interacting HFC molecules. In this case, $x_s = N_s/(N_{IL} + N_s)$, where N_{IL} is the number of IL ion pairs. To ensure adequate phase-space overlap between adjacent states, the two end states were connected with 22 alchemical intermediate states by slowly turning off the interactions between one HFC molecule and the remainder of the system. The potential energy is dependent on the coupling parameter λ ranging from 0.0 to 1.0. There were 24 different λ windows in total determined by both λ_{vdw} and λ_{coul}, the coupling parameters for van der Waals (VdW) and Coulombic interactions, respectively. Generally, it is more efficient to linearly turn off the Coulombic interactions before turning off the VdW interactions as shown in Figure S1.[40] For Coulombic interactions, a linear alchemical pathway was applied as follows:

$$U(\lambda_{coul}) = (1 - \lambda_{coul})U_A + \lambda_{coul}U_B \quad (5)$$

where U_A and U_B are the potential energies of states A and B, respectively. To avoid the end point singularity effect caused by the r^{-12} term in the Lennard-Jones potential, a soft-core version of the potential[41] was applied to VdW interactions:

$$U(r_{ij}, \lambda_{vdw}) = 4\epsilon_{ij}(1 - \lambda_{vdw})\left(\frac{1}{(\alpha\lambda_{vdw} + (r_{ij}/\sigma_{ij})^6)^2} - \frac{1}{\alpha\lambda_{vdw} + (r_{ij}/\sigma_{ij})^6}\right) \quad (6)$$

where α is the soft-core repulsive parameter set as 0.5, and σ is the soft-core attractive parameter equal to 0.3. Detailed λ parameters are documented in Table S1 and plotted in Figure S1.

As shown in Figure 3, a regular MD simulation was performed at each λ, and there were 24 λ windows simulated in parallel. Every 100 time steps, the total energy differences between all λ states was computed and written to a .xvg output file. Every 2000 time steps, configurations of different replicas were attempted to swap based on the Metropolis criterion.[42] The acceptance probability between two replicas i and j is

$$P(q_i \rightarrow q_j) = \min\left(1, \exp\left[-\frac{1}{k_B T}(U_i(q_j) + U_j(q_i) - U_i(q_i) - U_j(q_j))\right]\right) \quad (7)$$

where q_i and q_j are molecular configurations of two replicas i and j, and U_i and U_j are the potential energy functions of the corresponding replicas. A total of 1000 attempted exchanges was made for each swap, which was sampled according to Gibbs sampling.[43]

To give a sense of how well HREX does in sampling configurations of the solute molecule in an IL, Figure 4 depicts the situation where a single HFC-32 molecule is dissolved in

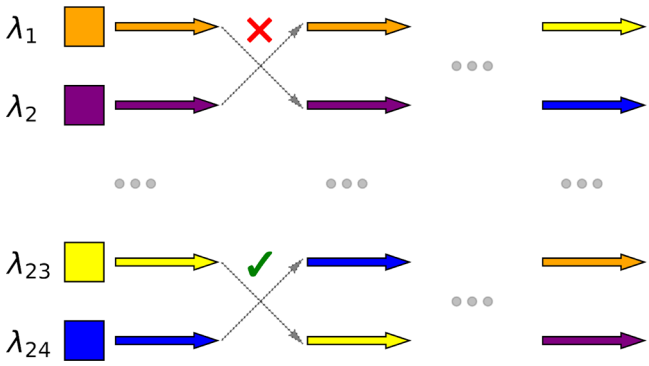

Figure 3. Graphical representation of HREX MD simulation. There are 24 λ states running in parallel, and every 2000 time steps, attempts are made to exchange coordinates of different replicas with Gibbs sampling. Exchanges are accepted or rejected based on the Metropolis rule. The green checkmark means this attempt is accepted, while the red cross represents that the attempt is denied. Square shapes with different colors are configurations that were initialized in different replicas. Arrows of different colors represent short simulation intervals.

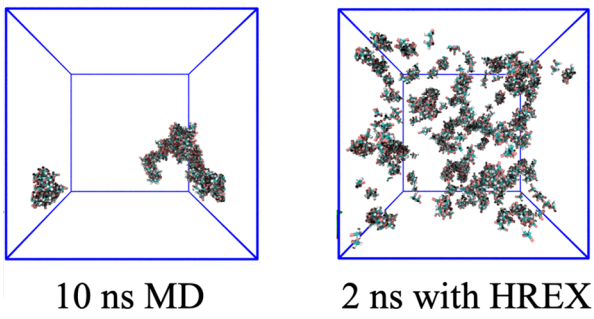

Figure 4. Depiction of the locations accessed by a single HFC-32 molecule over 10 ns of simulation time without HREX (left) and over 2 ns with HREX (right). The HFC molecule probes only a small fraction of the liquid phase without HREX, while with HREX it samples essentially the entire box, despite the fact that the simulation is 5 times shorter. $[C_4C_1im][PF_6]$ molecules are not shown for clarity.

$[C_4C_1im][PF_6]$. With normal MD, the HFC molecule only probes a small region of the liquid phase over 10 ns of simulation time, due to the solute being captured within an IL cavity and constrained by the sluggish IL dynamics. With HREX, however, the HFC molecule samples most of the liquid box volume over only 2 ns of simulation time. It is important to note that HREX does not improve sluggish IL dynamics, but rather allows the solute molecule to "jump" between different cavities within the IL and thus explore more configuration space in less simulation time.

Free Energy Estimators. Under the *NPT* ensemble, the Gibbs free energy is defined by

$$G(N_s, N_{IL}, P, T) = -k_B T \ln \Delta(N_s, N_{IL}, P, T) \quad (8)$$

where N_s is the number of solute (HFC) molecules in the liquid phase, N_{IL} is the number of solvent (IL) molecules, k_B is the Boltzmann constant, and Δ is the partition function. The Helmholtz free energy is defined in the same way but under the canonical (*NVT*) ensemble. To estimate the total free energy difference of adding a single HFC molecule to the IL, a family of analysis methods were applied to make fair cross-comparison.

https://doi.org/10.1021/acs.jctc.3c00206
J. Chem. Theory Comput. 2023, 19, 3324−3335

The first category is called thermodynamics integration (TI), where the simulated free energy difference between the initial and final state is

$$\Delta G_{\mathrm{sim}}(T, P, x_{\mathrm{s}}) = -k_{\mathrm{B}}T \ln\left[\frac{\Delta(N_{\mathrm{s}}, N_{\mathrm{IL}}, P, T, \lambda = 1)}{\Delta(N_{\mathrm{s}}, N_{\mathrm{IL}}, P, T, \lambda = 0)}\right] = -k_{\mathrm{B}}T \int_0^1 \mathrm{d}\lambda \frac{\mathrm{d} \ln \Delta(\lambda)}{\mathrm{d}\lambda} = \int_0^1 \mathrm{d}\lambda \left\langle \frac{\mathrm{d}H(\lambda)}{\mathrm{d}\lambda} \right\rangle_{N_{\mathrm{s}}, N_{\mathrm{IL}}, P, T, \lambda} \quad (9)$$

where "s" refers to solute while IL represents solvent, the angle brackets mean ensemble average, and H is the Hamiltonian. Since kinetic energy, the thermostat, and the barostat present no dependence on λ, the free energy difference can be written as

$$\Delta G_{\mathrm{sim}}(T, P, x_{\mathrm{s}}) = \int_0^1 \mathrm{d}\lambda \left\langle \frac{\mathrm{d}U(\lambda)}{\mathrm{d}\lambda} \right\rangle_{N_{\mathrm{s}}, N_{\mathrm{IL}}, P, T, \lambda} \quad (10)$$

Thus, the free energy difference can be obtained from the area of the $\left\langle \frac{\mathrm{d}U(\lambda)}{\mathrm{d}\lambda} \right\rangle_{\lambda}$ vs λ curve, as shown in Figure 5. The TI and

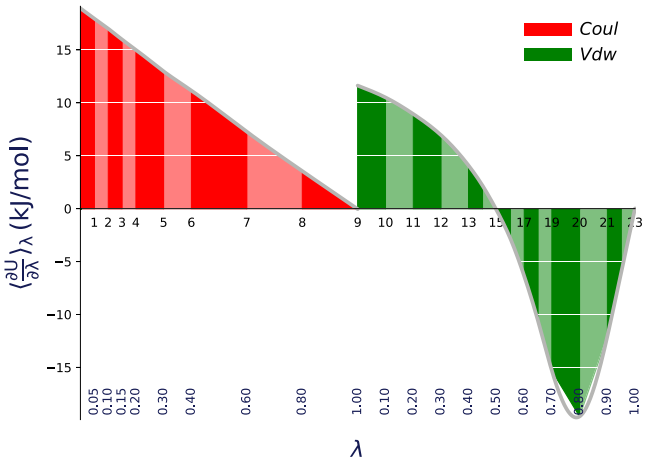

Figure 5. Derivative of the potential energy with respect to λ of HFC-32 in $[C_4C_1im][BF_4]$ at the highest concentration (N_s = 800) at 298.15 K and 1 bar. Free energy differences can be calculated using TI by estimating the red (Coulombic component) and green (VdW component) filled areas using the trapezoid rule. The silver curve is interpolated via cubic spline used for the TI-CUBIC method. This plot was generated using Alchemical Analysis.[40]

TI-CUBIC methods utilize the trapezoid rule and the cubic spline integration to estimate the area, respectively.[40] The drawback of TI is that the discrete λ spacing at a large curvature of $\left\langle \frac{\mathrm{d}U(\lambda)}{\mathrm{d}\lambda} \right\rangle_{\lambda}$ vs λ leads to significant quadrature bias, which causes difficulty in quantifying the estimation (see void space in the green area in Figure 5).

The second kind of estimator is called the free energy perturbation method, shortened as FEP or EXP. According to the direction of the transformation, EXP can be divided into deletion EXP (DEXP) and insertion EXP (IEXP), which proceed in the directions of increasing and decreasing entropy, respectively.[40] Based on the methodology initially introduced by Zwanzig,[44] the Gibbs free energy difference of two states i and j is

$$\Delta G = -\frac{1}{\beta} \ln\langle \exp(-\beta \Delta U)\rangle_i = \frac{1}{\beta} \ln\langle \exp(-\beta \Delta U)\rangle_j \quad (11)$$

where ΔU is the potential energy difference between the states i and j and $\beta = \frac{1}{k_{\mathrm{B}}T}$. This equation is only applicable if states i and j share adequate overlap in phase space. To deal with large perturbations, multiple simulations of intermediate state are required to obtain an accurate estimation, called the stratification strategy.[45] The total Gibbs free energy difference between the initial (A) and final (B) states is

$$\Delta G_{\mathrm{sim}} = -k_{\mathrm{B}}T \sum_{i=1}^{N-1} \ln\langle e^{-[U(\lambda_{i+1}) - U(\lambda_i)]/k_{\mathrm{B}}T}\rangle_i \quad (12)$$

where N is the number of λ windows.

The multistate Bennett acceptance ratio (MBAR) method[46] is considered as an unbiased free energy estimator with the lowest variance.[47] The basic idea is to solve a set of K (the total number of states) estimating equations simultaneously and use extended bridge sampling[48] to calculate free energies with the lowest variance. The overlap matrix in Figure 6 provides a quantitative measurement of the phase-space overlap. The element O_{ij} represents the average probability of finding a sample collected from state i (row) having been generated from state j (column):

$$O_{ij} = \left\langle \frac{N_i p_i(\mathbf{x})}{\sum_{k=1}^{K} N_k p_k(\mathbf{x})} \right\rangle_j \quad (13)$$

where N_i and N_k are the numbers of samples collected from probability distributions $p_i(\mathbf{x})$ and $p_k(\mathbf{x})$, respectively.[40]

To ensure overlap in phase space, elements in the upper and lower diagonals of the overlap matrix should be sufficiently larger than 0, and elements in the main diagonal should be less than 1. This indicates phase-space overlap between neighboring λ states. Nonzero probabilities outside of the tridiagonal indicate overlap between the phase spaces of further separated λ states. As shown in Figure 6, the wide band between states 0 and 8 indicates strong overlap and easy transitions between λ states when turning off the Coulombic interactions. The wide band of relatively low probabilities is a sign of an excess number of λ states in this region and suggests an opportunity to optimize the number and spacing of λ states in the future. For λ windows numbered 9 and higher, the electrostatic interactions have been turned completely off. In general, the more concentrated transition probabilities along the tridiagonal of λ windows 9 and higher indicate somewhat lesser phase-space overlap while the VDW interactions are turned off, though the overlap remains more than sufficient to ensure easy transitions between neighboring λ states.

The Bennett acceptance ratio (BAR) method[49] is a special case of MBAR that deals with two states instead of multiple states at a time.

All the algorithms of estimators mentioned above are implemented in the Alchemical Analysis tool[40] and the pymbar[50] package. Statistical tests have proved that MBAR shows the highest accuracy of free energy estimates and highest reliability of uncertainty analysis among these six methods.[51] Thus, we will use free energy estimates from MBAR for solubility estimations.

https://doi.org/10.1021/acs.jctc.3c00206
J. Chem. Theory Comput. 2023, 19, 3324−3335

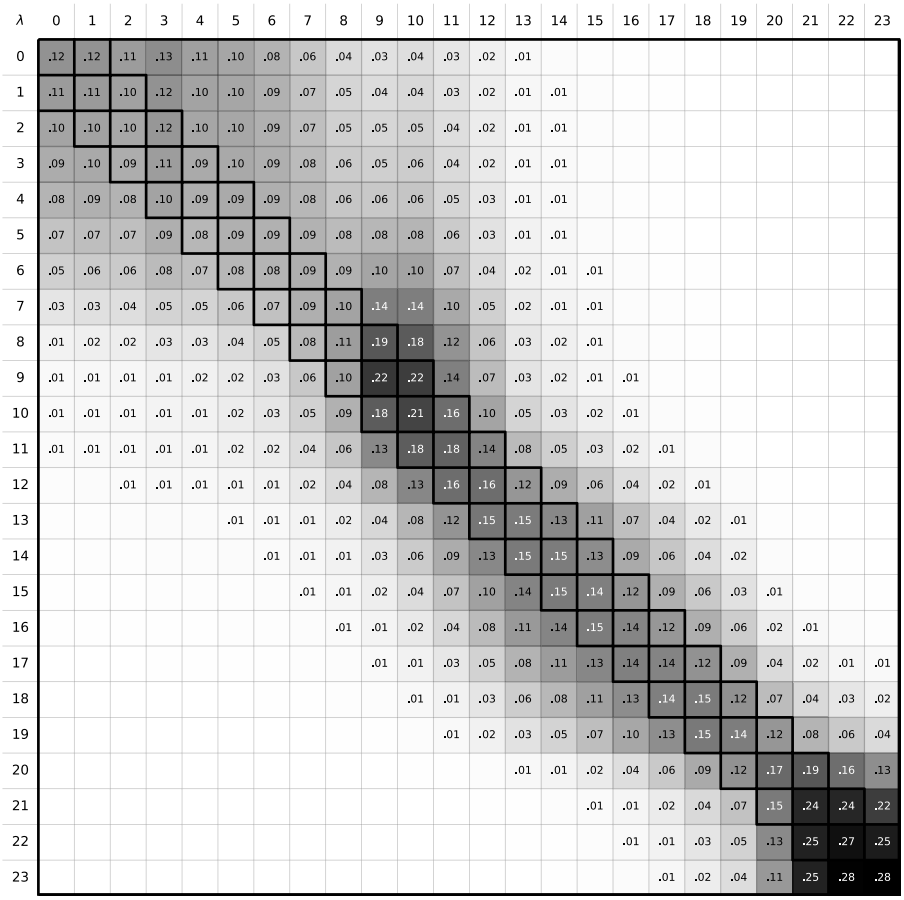

Figure 6. Overlap matrix of HFC-32 in $[C_4C_1im][BF_4]$ at the highest concentration (N_s = 800) at 298.15 K and 1 bar. Darker shades correspond to higher probabilities. This plot was generated using Alchemical Analysis.[40]

RESULT AND DISCUSSION

Convergence Assessment. A basic rule to assess the equilibrium of a simulation is to check the convergence plot of free energy differences versus time as shown in Figure 7. As stated in ref 40, the forward and reverse data should rapidly converge to a range within uncertainty from the opposite direction. The range of the *y*-axis in Figure 7 is small enough to conclude that our production data are well equilibrated.

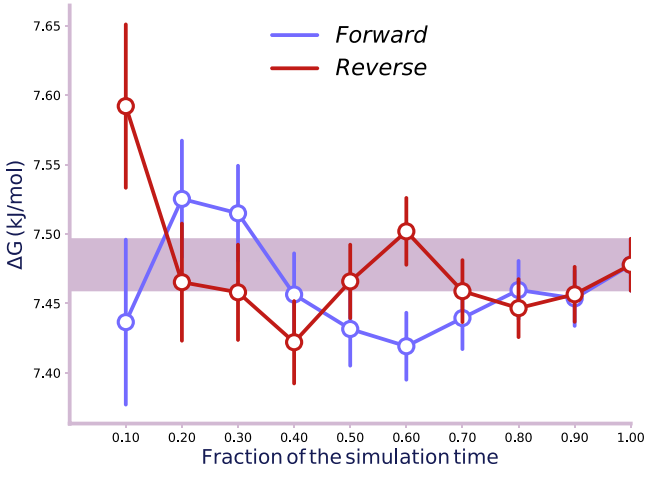

Figure 7. Convergence plot of free energy difference versus time of HFC-32 in $[C_4C_1im][BF_4]$ at the highest concentration (N_s = 800) at 298.15 K and 1 bar. Forward and reverse mean free energy estimates were calculated from the normal and time-reversed data, respectively. This plot was generated using Alchemical Analysis.[40]

Cross-Comparison. Multiple analysis methods were applied to calculate the total Gibbs free energy difference between the two end states. Inconsistency between different methods implies unreasonable chosen spacing of λ values and insufficient sampling.[40] As shown in Figure S2, free energy estimates are consistent between different methods and the error bar for each method is small. Sometimes, estimates from IEXP and DEXP can be inconsistent even if the sampling is sufficient to provide accurate results from other methods. Therefore, we primarily focus on the agreement between TI-based methods and BAR-based methods.[40]

Equation of State (EOS). Previous investigations have shown that the VdW EOS[52] and PR EOS[53] are good fits for correlating experimental data and modeling the solubility of the HFCs in the ILs, which motivates us to utilize the PR EOS to obtain the excess chemical potential versus the pressure of HFCs in the vapor phase. To test the feasibility of using the PR EOS from REFPROP, comparison was made between the PR EOS, the VdW EOS, and HREX MD simulations. In the PR model, the excess chemical potential of vapor HFCs, μ_{ex}, is $RT \ln(\phi)$ as stated before, where ϕ is the fugacity coefficient. Thus, the data points of ϕ vs P obtained from REFPROP can be easily converted into μ_{ex} vs P.

The fugacity coefficient can also be computed from the VdW EOS:

https://doi.org/10.1021/acs.jctc.3c00206
J. Chem. Theory Comput. 2023, 19, 3324−3335

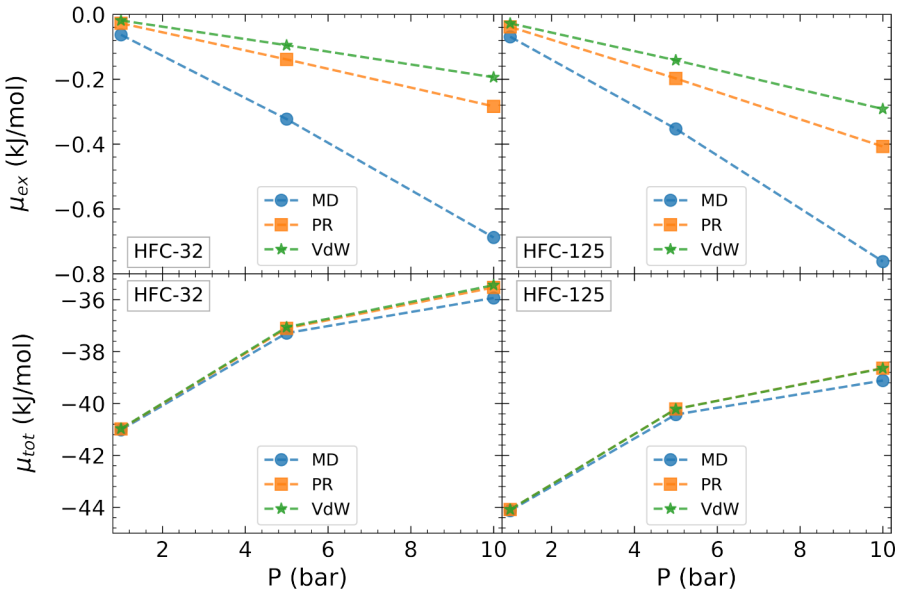

Figure 8. Excess chemical potential (top) and total chemical potential (below) of vapor HFC-32 (left) and vapor HFC-125 (right) as a function of pressure at 298.15 K estimated by HREX MD simulations (blue), PR EOS (orange), and VdW EOS (green).

$$\ln(\phi) = \frac{b}{V_m - b} - \frac{2a}{RTV_m} + \ln\left(\frac{RT}{P(V_m - b)}\right) \quad (14)$$

where $a = \frac{27R^2T_c^2}{64P_c}$, $b = \frac{RT_c}{8P_c}$, and V_m can be solved through the VdW equation of state

$$P = \frac{RT}{V_m - b} - \frac{a}{V_m^2}$$

given the temperature (T) and pressure (P). R is the gas constant, T_c is the critical temperature, and P_c is the critical pressure.[54] Once the relationship between ϕ and P is obtained, we used the same procedure as before to get μ_{ex} vs P.

HREX MD simulations were then employed to compute the excess chemical potential of both vapor HFC-32 and vapor HFC-125 at 1, 5, and 10 bar. One hundred HFC molecules were placed inside a box whose initial size was determined by the ideal gas law $V = \frac{nRT}{P}$. The simulation setup and procedure follow the same details as mentioned under Simulation Methods, and the chemical potential was determined from the excess Gibbs energy.

As shown in Figure 8, excess chemical potential estimates from the PR EOS are slightly larger (more negative) than those from the VdW EOS and smaller than estimates from the MD simulations. These differences become more significant as the pressure increases. Numerical values of the chemical potential are documented in Table S2 in detail. Since the value of the ideal chemical potential is much larger than the excess component, however, the total chemical potentials are similar between the different methods. Thus, the choice of EOS or MD simulations presents a relatively small effect on the chemical potential at these pressures.

From HREX MD simulations, we can calculate the excess and total chemical potential in the liquid phase at certain HFC concentrations. The next step is to linearly interpolate the pressure versus total chemical potential curve in the vapor phase to find the corresponding equilibrium pressure. We take HFCs in the $[C_4C_1im][BF_4]$ binary system as an example and use the pressure versus chemical potential curves from PR EOS, VdW EOS, and HREX MD simulations to estimate the final solubility isotherms. As shown in Figure S3, the equilibrium pressures of HFC-32 and HFC-125 in $[C_4C_1im][BF_4]$ estimated from MD agree very well with EOS methods at low pressure, and there are small deviations at higher pressure. Detailed values are documented in Table S3. Thus, the final solubility data points show little dependence on the EOS or MD methods at relatively low pressures.

However, the computational times to perform these calculations are vastly different. For example, the wall-clock times of a single λ window for a 50 ns HREX MD production run of vapor HFC-32 and HFC-125 at 298.15 K and 10 bar are ~25 and ~28 h, respectively. The corresponding CPU times of HFC-32 and HFC-125 are 202 and 223 h, respectively. While this is not the most efficient way of computing gas phase chemical potentials, it demonstrates that there is significant overhead in computing chemical potentials compared to evaluating them via an EOS (which is essentially instantaneous). Given that the PR EOS can provide us with precise estimates according to Figure 8, and the fact that μ_{ex} vs P data points at various temperatures can be conveniently obtained from REFPROP, we concluded that it was reasonable to use the PR EOS for gas phase chemical potentials.

Solubility Isotherms. Figure 9 compares the simulated solubility of HFC-32 in $[C_4C_1im][PF_6]$ as calculated with the HREX and GEMC methods. HREX predictions agree perfectly well with the GEMC result, while the latter took 3 months to converge to an accurate value. Encouragingly, the wall-clock time of HREX varies from 3 to 4 days for a data point on the isotherm, depending on the concentration and system. From a CPU standpoint, since 24 λ windows were running in parallel for 50 ns during the production stage, the overall CPU time is ~1.5−2 years for a single point on the isotherm. Due to parallel computing, however, the HREX method is much faster than the traditional GEMC method in terms of wall-clock time. Solubility results from different simulation lengths (10, 30, and 50 ns) are compared in Figure S4 with detailed numbers in Table S4. Deviations between different simulation lengths

https://doi.org/10.1021/acs.jctc.3c00206
J. Chem. Theory Comput. 2023, 19, 3324−3335

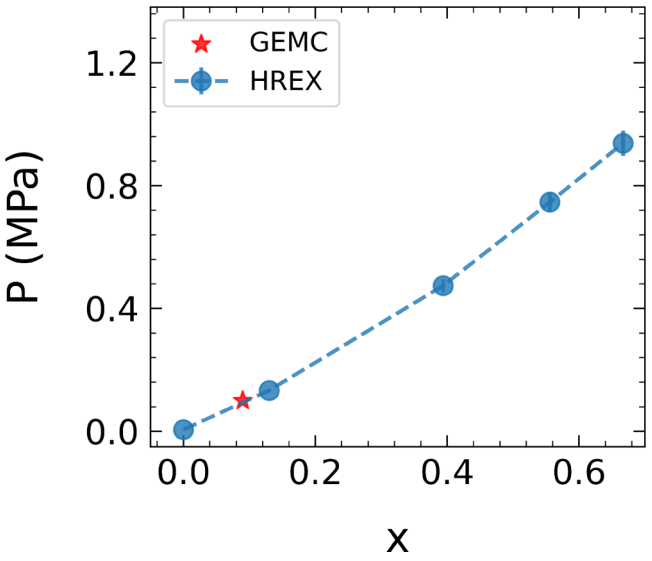

Figure 9. Simulated solubility data from HREX (blue) and from GEMC (red) of HFC-32 in $[C_4C_1im][PF_6]$ at 298.15 K.

became evident at high pressure. A longer simulation time leads to more accurate results relative to the experiment and smaller error bars predicted from MBAR. For our initial studies presented here, we ran 50 ns production simulations to ensure high accuracy results. Further investigation is underway to improve the efficiency of this workflow by optimizing the number of λ states, λ spacing, and simulation length.

Solubility isotherms of HFC-32 and HFC-125 in $[C_4C_1im][BF_4]$, $[C_4C_1im][PF_6]$, and $[C_4C_1im][SCN]$ were calculated and are compared with experimental results[52] in Figure 10. Pressures that exceed the vapor pressure of HFC at 298.15 K were excluded. Since only two data points were left for HFC-125 in the $[C_4C_1im][SCN]$ mixture, we added a simulation at x = 0.07 for this specific system. Detailed values of the simulation results are documented in Table S5. The HREX MD simulations slightly overestimate the solubility of HFC-32 in the ILs and nearly perfectly estimate the solubility of HFC-125. The simulations also capture the solubility trend and the curvature of the isotherms. As described in ref 33, the charge scaling factor on the IL is set as 0.8 to account for charge transfer and the polarization effect. We suspect that the relatively larger deviation of simulated HFC-32 solubility is caused by the bigger influence of the nonpolarizable classical IL force field on more polar HFC-32 molecules. Future work will be conducted on developing a GAFF-based polarizable force field of ILs and how IL polarization inclusion affects HFC solubility.

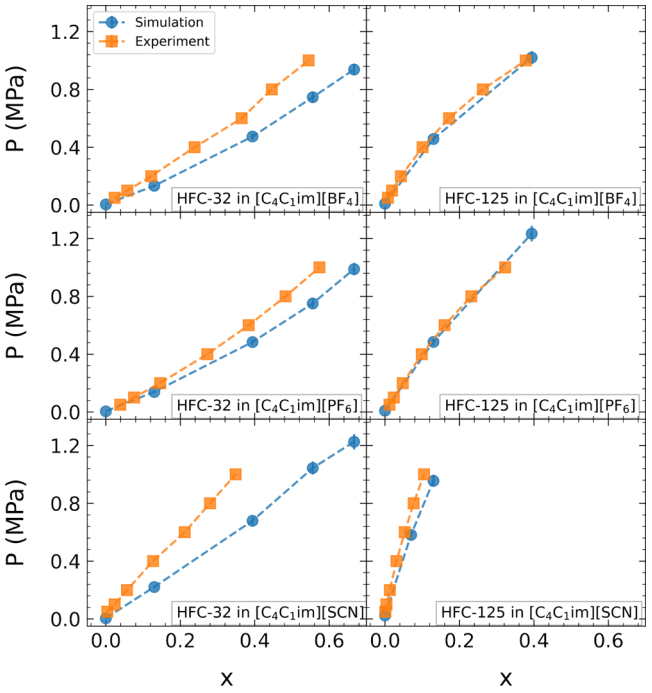

Figure 10. Simulated (blue) and experimental[52] (orange) solubility isotherms of HFC-32 (left) and HFC-125 (right) in $[C_4C_1im][BF_4]$, $[C_4C_1im][PF_6]$, and $[C_4C_1im][SCN]$ at 298.15 K.

To extend the method and elucidate the effect of the length of the cation alkyl chain on solubility, the binary systems of HFC-32 and HFC-125 with another IL, $[C_6C_1im][BF_4]$, were also studied. To validate the reliability of the force field parameters, the density and shear viscosity of pure $[C_6C_1im][BF_4]$ were first calculated. The density results are included in Figure 11 and compared with available experimental results.[55]

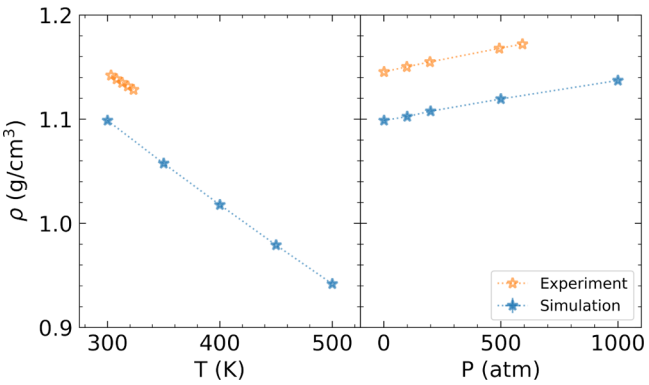

Figure 11. Simulated (blue) and experimental (orange) densities of pure $[C_6C_1im][BF_4]$ as a function of temperature (left) at 1 atm and pressure (right) at 300 K.

The average deviation from experimental values is −4.2%. Detailed values are documented in Table S6. The corresponding simulated isobaric expansivity (α) is 0.00077 K^{-1}, while the experimental value is 0.000602 K^{-1}. The corresponding simulated isothermal compressibility (κ) is 0.000339 MPa^{-1}, whereas the experimental value is 0.000381 MPa^{-1}. The deviations between simulation and experiment for α and κ are 28 and −11%, respectively. As shown in Table 1, the calculated viscosity agrees with experimental data reasonably well. Given that the IL force field seems reasonable, we then set out to predict the solubility isotherms. Figure 12 shows the results.

Table 1. Simulated and Experimental Viscosities and Corresponding Standard Deviations of Pure $[C_6C_1im][BF_4]$ at 300 K and 1 atm

experiment			simulation	
η (mPa·s)	$\bar{\eta}$ (mPa·s)	σ (mPa·s)	η (mPa·s)	σ (mPa·s)
209.4[58]				
168.1[55]	195.9	22.0	144.8	14
182.2[59]				
224.0[60]				

https://doi.org/10.1021/acs.jctc.3c00206
J. Chem. Theory Comput. 2023, 19, 3324−3335

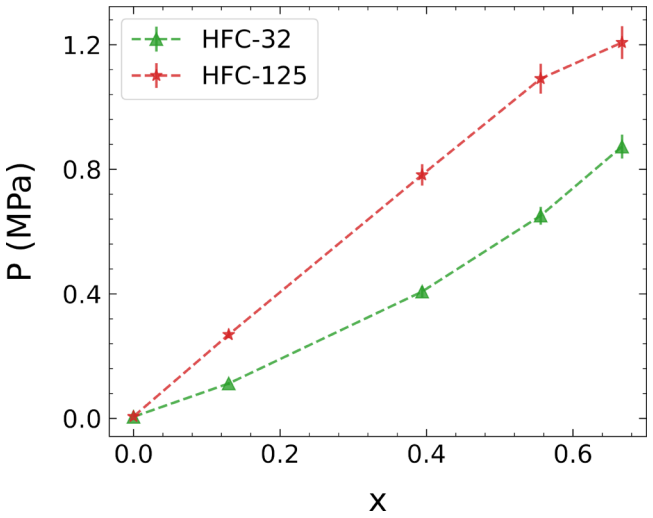

Figure 12. Simulated solubility isotherms of HFC-32 (green) and HFC-125 (red) in $[C_6C_1im][BF_4]$ at 298.15 K.

The simulations predict that HFC-32 is more soluble in $[C_6C_1im][BF_4]$ than HFC-125 is, which is consistent with the Henry's law constant trend observed in ref 56. As shown in Table S5, a longer cation alkyl chain results in higher solubilities of both HFC-32 and HFC-125 in ILs, which is expected and also observed for other HFC/IL systems.[57] So far, there are no experimentally measured isotherms for this system.

Henry's Law Constants. HREX MD simulations can also be used to predict the Henry's law constants of HFCs in ILs in the dilute limit according to eq 4. Detailed values are documented in Table 2. Five replicates of HFC-125 in $[C_4C_1im][BF_4]$ at the infinitely dilute concentration ($N_s = 0$) with different initial configurations were simulated independently. The standard deviation of results from these five independent simulations was considered as the uncertainty and propagated to other binary systems with the same relative uncertainty $\delta = \sigma/\bar{H}$ (see Table 3). The uncertainty obtained from five replicates was found to be slightly larger than that estimated from the Alchemical Analysis tool.[40] The experimental results for Henry's constants of HFCs in $[C_6C_1im][BF_4]$ in Table 2 were extrapolated from ref 56 using the enthalpy of absorption, $\Delta h = R\left(\frac{\partial \ln H}{\partial(1/T)}\right)_P$, where H is Henry's constant, R is the gas constant, T is temperature, and P is pressure. MD simulations capture the solubility trend that HFC-32 is more soluble in these four ILs than HFC-125 is and provide a small but systematic underestimation of Henry's law constants relative to experiments, i.e., overestimate the solubility of HFCs in ILs. Longer cation alkyl chains lead to higher solubility and lower selectivity.

Table 2. Detailed Henry's Law Constants for HFC-32 and HFC-125 in $[C_4C_1im][BF_4]$, $[C_4C_1im][PF_6]$, $[C_4C_1im][SCN]$, and $[C_6C_1im][BF_4]$ at 298.15 K Compared with Available Experimental Results[52,56a]

	$H_{HFC\text{-}32}$ (MPa)	$H^{Expt}_{HFC\text{-}32}$ (MPa)	$H_{HFC\text{-}125}$ (MPa)	$H^{Expt}_{HFC\text{-}125}$ (MPa)
$[C_4C_1im][BF_4]$	0.93_3	1.54	4.1_1	4.19
$[C_4C_1im][PF_6]$	0.94_3	1.34	3.4_1	4.05
$[C_4C_1im][SCN]$	1.52_4	3.11	9.7_3	13.32
$[C_6C_1im][BF_4]$	0.73_2	1.28	2.17_6	2.80

[a]The subscript is the uncertainty to the last digit.

Table 3. Uncertainty Analysis Performed on the Excess Chemical Potential, Henry's Law Constant, and Pressure of HFC-125 in $[C_4C_1im][BF_4]$ at 298.15 K in the Dilute Limit

trial	μ_{ex} (kJ/mol)	H (MPa)	P (MPa)
1	−2.80	4.06	0.0100
2	−2.87	3.95	0.0100
3	−2.69	4.25	0.0110
4	−2.82	4.03	0.0100
5	−2.77	4.11	0.0100
avg	−2.79	4.08	0.0102
σ	0.07	0.11	0.0004
δ	−0.02	0.03	0.0438

CONCLUSION

An alchemical free energy calculation method combined with HREX MD simulations was described and used to compute the full solubility isotherms of HFCs in ILs. The method requires substantially less wall-clock time than conventional Gibbs ensemble Monte Carlo simulations due to the highly parallelized nature of the HREX simulations. A single state point on a solubility isotherm required 3−4 days of wall-clock time for HREX compared with 3 months for GEMC. Although the calculations in this work required a large amount of CPU time (~1.5−2 years for a single point on the isotherm), future work will focus on improving the efficiency of this workflow by optimizing the number and spacing of λ states[61] and minimizing the length of production simulations. The simulated solubility isotherms can capture the experimental curvature and solubility trends reasonably well. Convergence checks ensured the equilibration of the production run. Various free energy estimation methods were cross-compared and presented consistent results and small uncertainties. The PR model from REFPROP was shown to be a reasonable and efficient way to calculate the excess chemical potentials of HFCs in the vapor phase. Overall, this workflow is considered as a precise method that can estimate full isotherms, can help discover the ideal IL candidate for the efficient separation of HFCs, and can facilitate future free energy studies for other systems.

ASSOCIATED CONTENT

Data Availability Statement

The code of this workflow is available to the public at https://github.com/MaginnGroup/HREX-workflow-source-code, including example GROMACS files; scripts of workflow; example Cassandra files for GEMC simulations.

Supporting Information

The Supporting Information is available free of charge at https://pubs.acs.org/doi/10.1021/acs.jctc.3c00206.

GEMC simulation details, plot of λ windows, cross-comparison between different free energy estimators and solubility isotherms; numerical values of λ windows, density, chemical potential, and solubility isotherm (PDF)

https://doi.org/10.1021/acs.jctc.3c00206
J. Chem. Theory Comput. 2023, 19, 3324−3335

AUTHOR INFORMATION

Corresponding Author

Edward J. Maginn − *Department of Chemical and Biomolecular Engineering, University of Notre Dame, Notre Dame, Indiana 46556, United States;* orcid.org/0000-0002-6309-1347; Email: ed@nd.edu

Authors

Ning Wang − *Department of Chemical and Biomolecular Engineering, University of Notre Dame, Notre Dame, Indiana 46556, United States;* orcid.org/0000-0002-5515-6198

Ryan S. DeFever − *Department of Chemical and Biomolecular Engineering, University of Notre Dame, Notre Dame, Indiana 46556, United States;* orcid.org/0000-0001-5311-6718

Complete contact information is available at: https://pubs.acs.org/10.1021/acs.jctc.3c00206

Author Contributions

†N.W. and R.S.D. contributed equally.

Notes

The authors declare no competing financial interest.

ACKNOWLEDGMENTS

The authors are thankful for the financial support provided by the National Science Foundation, EFRI DChem: Next-generation Low Global Warming Refrigerants, Award No. 2029354, and the computing resources from the Center for Research Computing (CRC) at the University of Notre Dame.

REFERENCES

(1) Wilkes, J. S.; Wasserscheid, P.; Welton, T. *Ionic Liquids in Synthesis*; John Wiley & Sons, Ltd.: 2007; Chapter 1, pp 1−6.

(2) Shiflett, M. B.; Magee, J. W.; Tuma, D. In *Commercial Applications of Ionic Liquids*; Shiflett, M. B., Ed.; Springer International Publishing: Cham, Switzerland, 2020; pp 3−29.

(3) Shiflett, M. B.; Maginn, E. J. The Solubility of Gases in Ionic Liquids. *AIChE J.* **2017**, *63*, 4722−4737.

(4) Lei, Z.; Dai, C.; Chen, B. Gas Solubility in Ionic Liquids. *Chem. Rev.* **2014**, *114*, 1289−1326.

(5) Yokozeki, A. Solubility Correlation and Phase Behaviors of Carbon Dioxide and Lubricant Oil Mixtures. *Appl. Energy* **2007**, *84*, 159−175.

(6) Lynden-Bell, R. M.; Atamas, N. A.; Vasilyuk, A.; Hanke, C. G. Chemical Potentials of Water and Organic Solutes in Imidazolium Ionic Liquids: A Simulation Study. *Mol. Phys.* **2002**, *100*, 3225−3229.

(7) Shah, J. K.; Maginn, E. J. A Monte Carlo Simulation Study of the Ionic Liquid 1-n-butyl-3-methylimidazolium Hexafluorophosphate: Liquid Structure, Volumetric Properties and Infinite Dilution Solution Thermodynamics of CO_2. *Fluid Phase Equilib.* **2004**, *222−223*, 195−203.

(8) Shah, J. K.; Maginn, E. J. Monte Carlo Simulations of Gas Solubility in the Ionic Liquid 1-n-Butyl-3-methylimidazolium Hexafluorophosphate. *J. Phys. Chem. B* **2005**, *109*, 10395−10405.

(9) Liu, H.; Dai, S.; Jiang, D. Solubility of Gases in a Common Ionic Liquid from Molecular Dynamics Based Free Energy Calculations. *J. Phys. Chem. B* **2014**, *118*, 2719−2725.

(10) Zheng, W.; Zheng, L.; Sun, W.; Zhao, L. Screening of Imidazolium Ionic Liquids for the Isobutane Alkylation Based on Molecular Dynamic Simulation. *Chem. Eng. Sci.* **2018**, *183*, 115−122.

(11) Salehin, F. N. M.; Jumbri, K.; Ramli, A.; Daud, S.; Abdul Rahman, M. B. In Silico Solvation Free Energy and Thermodynamics Properties of H_2S in Cholinium-based Amino Acid Ionic Liquids. *J. Mol. Liq.* **2019**, *294*, 111641.

(12) Asensio-Delgado, S.; Viar, M.; Padua, A. A.; Zarca, G.; Urtiaga, A. Understanding the Molecular Features Controlling the Solubility Differences of R-134a, R-1234ze(E), and R-1234yf in 1-Alkyl-3-methylimidazolium Tricyanomethanide Ionic Liquids. ACS Sustainable. *Chem. Eng.* **2022**, *10*, 15124−15134.

(13) Urukova, I.; Vorholz, J.; Maurer, G. Solubility of CO_2, CO, and H_2 in the Ionic Liquid [bmim][PF_6] from Monte Carlo Simulations. *J. Phys. Chem. B* **2005**, *109*, 12154−12159.

(14) Shi, W.; Maginn, E. J. Atomistic Simulation of the Absorption of Carbon Dioxide and Water in the Ionic Liquid 1-n-Hexyl-3-methylimidazolium Bis(trifluoromethylsulfonyl)imide ([hmim][Tf_2N]. *J. Phys. Chem. B* **2008**, *112*, 2045−2055.

(15) Shi, W.; Maginn, E. J. Molecular Simulation and Regular Solution Theory Modeling of Pure and Mixed Gas Absorption in the Ionic Liquid 1-n-Hexyl-3-methylimidazolium Bis(Trifluoromethylsulfonyl)amide ([hmim][Tf_2N]). *J. Phys. Chem. B* **2008**, *112*, 16710−16720.

(16) Singh, R.; Marin-Rimoldi, E.; Maginn, E. J. A Monte Carlo Simulation Study To Predict the Solubility of Carbon Dioxide, Hydrogen, and Their Mixture in the Ionic Liquids 1-Alkyl-3-methylimidazolium bis(trifluoromethanesulfonyl)amide ([Cnmim+][Tf2N-], n = 4, 6). *Ind. Eng. Chem. Res.* **2015**, *54*, 4385−4395.

(17) Becker, T. M.; Wang, M.; Kabra, A.; Jamali, S. H.; Ramdin, M.; Dubbeldam, D.; Infante Ferreira, C. A.; Vlugt, T. J. H. Absorption Refrigeration Cycles with Ammonia-Ionic Liquid Working Pairs Studied by Molecular Simulation. *I & EC Res.* **2018**, *57*, 5442−5452.

(18) Pohorille, A.; Jarzynski, C.; Chipot, C. Good Practices in Free-Energy Calculations. *J. Phys. Chem. B* **2010**, *114*, 10235−10253.

(19) Bannan, C. C.; Calabró, G.; Kyu, D. Y.; Mobley, D. L. Calculating Partition Coefficients of Small Molecules in Octanol/Water and Cyclohexane/Water. *J. Chem. Theory Comput.* **2016**, *12*, 4015−4024.

(20) Bussi, G. Hamiltonian Replica Exchange in GROMACS: A Flexible Implementation. *Mol. Phys.* **2014**, *112*, 379−384.

(21) Fukunishi, H.; Watanabe, O.; Takada, S. On the Hamiltonian Replica Exchange Method for Efficient Sampling of Biomolecular Systems: Application to Protein Structure Prediction. *J. Chem. Phys.* **2002**, *116*, 9058−9067.

(22) Woods, C. J.; Essex, J. W.; King, M. A. Enhanced Configurational Sampling in Binding Free-Energy Calculations. *J. Phys. Chem. B* **2003**, *107*, 13711−13718.

(23) Jiang, W.; Roux, B. Free Energy Perturbation Hamiltonian Replica-Exchange Molecular Dynamics (FEP/H-REMD) for Absolute Ligand Binding Free Energy Calculations. *J. Chem. Theory Comput.* **2010**, *6*, 2559−2565.

(24) Affentranger, R.; Tavernelli, I.; Di Iorio, E. E. A Novel Hamiltonian Replica Exchange MD Protocol to Enhance Protein Conformational Space Sampling. *J. Chem. Theory Comput.* **2006**, *2*, 217−228.

(25) Meng, Y.; Sabri Dashti, D.; Roitberg, A. E. Computing Alchemical Free Energy Differences with Hamiltonian Replica Exchange Molecular Dynamics (H-REMD) Simulations. *J. Chem. Theory Comput.* **2011**, *7*, 2721−2727.

(26) Shah, J. K.; Marin-Rimoldi, E.; Mullen, R. G.; Keene, B. P.; Khan, S.; Paluch, A. S.; Rai, N.; Romanielo, L. L.; Rosch, T. W.; Yoo, B.; et al. Cassandra: An Open Source Monte Carlo Package for Molecular Simulation. *J. Comput. Chem.* **2017**, *38*, 1727−1739.

(27) Shirts, M. R.; Pitera, J. W.; Swope, W. C.; Pande, V. S. Extremely Precise Free Energy Calculations of Amino Acid Side Chain Analogs: Comparison of Common Molecular Mechanics Force Fields for Proteins. *J. Chem. Phys.* **2003**, *119*, 5740−5761.

(28) Befort, B. J.; DeFever, R. S.; Tow, G. M.; Dowling, A. W.; Maginn, E. J. Machine Learning Directed Optimization of Classical Molecular Modeling Force Fields. *J. Chem. Inf. Model.* **2021**, *61*, 4400−4414.

(29) Lemmon, E. W.; Bell, I.; Huber, M. L.; McLinden, M. O. *NIST Standard Reference Database 23: Reference Fluid Thermodynamic and Transport Properties-REFPROP: Version 10*. National Institute of Standards and Technology. 2018. https://www.nist.gov/srd/refprop.

(30) Wu, H.; Maginn, E. J. Water Solubility and Dynamics of CO_2 Capture Ionic Liquids Having Aprotic Heterocyclic Anions. *Fluid Phase Equilib.* **2014**, *368*, 72−79.
(31) Wang, J.; Wolf, R. M.; Caldwell, J. W.; Kollman, P. A.; Case, D. A. Development and Testing of a General Amber Force Field. *J. Comput. Chem.* **2004**, *25*, 1157−1174.
(32) Leach, A. *Molecular Modelling: Principles and Applications*; Prentice Hall: 2001.
(33) Wang, N.; Zhang, Y.; Al-Barghouti, K. S.; Kore, R.; Scurto, A. M.; Maginn, E. J. Structure and Dynamics of Hydrofluorocarbon/Ionic Liquid Mixtures: An Experimental and Molecular Dynamics Study. *J. Phys. Chem. B* **2022**, *126*, 8309−8321.
(34) Abraham, M. J.; Murtola, T.; Schulz, R.; Páll, S.; Smith, J. C.; Hess, B.; Lindahl, E. GROMACS: High Performance Molecular Simulations Through Multi-Level Parallelism From Laptops to Supercomputers. *SoftwareX* **2015**, *1*, 19−25.
(35) Van Gunsteren, W. F.; Berendsen, H. J. C. A Leap-frog Algorithm for Stochastic Dynamics. *Mol. Simul.* **1988**, *1*, 173−185.
(36) Goga, N.; Rzepiela, A. J.; de Vries, A. H.; Marrink, S. J.; Berendsen, H. J. C. Efficient Algorithms for Langevin and DPD Dynamics. *J. Chem. Theory Comput.* **2012**, *8*, 3637−3649.
(37) Berendsen, H. J. C.; Postma, J. P. M.; van Gunsteren, W. F.; DiNola, A.; Haak, J. R. Molecular Dynamics with Coupling to an External Bath. *J. Chem. Phys.* **1984**, *81*, 3684−3690.
(38) Parrinello, M.; Rahman, A. Polymorphic Transitions in Single Crystals: A New Molecular Dynamics Method. *J. Appl. Phys.* **1981**, *52*, 7182−7190.
(39) Darden, T.; York, D.; Pedersen, L. Particle Mesh Ewald: An Nlog(N) Method for Ewald Sums in Large Systems. *J. Chem. Phys.* **1993**, *98*, 10089−10092.
(40) Mobley, D.; Klimovich, P.; Shirts, M. Guidelines for the Analysis of Free Energy Calculations. *J. Comput.-Aided Mol. Des.* **2015**, *29*, 397−411.
(41) Beutler, T. C.; Mark, A. E.; van Schaik, R. C.; Gerber, P. R.; van Gunsteren, W. F. Avoiding Singularities and Numerical Instabilities in Free Energy Calculations Based on Molecular Simulations. *Chem. Phys. Lett.* **1994**, *222*, 529−539.
(42) Metropolis, N.; Rosenbluth, A. W.; Rosenbluth, M. N.; Teller, A. H.; Teller, E. Equation of State Calculations by Fast Computing Machines. *J. Chem. Phys.* **1953**, *21*, 1087−1092.
(43) Chodera, J. D.; Shirts, M. R. Replica Exchange and Expanded Ensemble Simulations as Gibbs Sampling: Simple Improvements for Enhanced Mixing. *J. Chem. Phys.* **2011**, *135*, 194110.
(44) Zwanzig, R. W. High-Temperature Equation of State by a Perturbation Method. I. Nonpolar Gases. *J. Chem. Phys.* **1954**, *22*, 1420−1426.
(45) Chipot, C.; Pohorille, A. In *Free Energy Calculations: Theory and Applications in Chemistry and Biology*; Chipot, C., Pohorille, A., Eds.; Springer: Berlin, 2007; pp 33−75.
(46) Shirts, M. R.; Chodera, J. D. Statistically Optimal Analysis of Samples from Multiple Equilibrium States. *J. Chem. Phys.* **2008**, *129*, 124105.
(47) Shirts, M. R. Reweighting from the Mixture Distribution as a Better Way to Describe the Multistate Bennett Acceptance Ratio. *arXiv (Condensed Matter.Statistical Mechanics)*, December 19, 2017, 1704.00891, ver. 4. https://arxiv.org/abs/1704.00891.
(48) Tan, Z. On a Likelihood Approach for Monte Carlo Integration. *J. Am. Stat. Assoc.* **2004**, *99*, 1027−1036.
(49) Bennett, C. H. Efficient Estimation of Free Energy Differences from Monte Carlo Data. *J. Comput. Phys.* **1976**, *22*, 245−268.
(50) *Pymbar Package*. http://github.com/choderalab/pymbar.
(51) Paliwal, H.; Shirts, M. R. A Benchmark Test Set for Alchemical Free Energy Transformations and Its Use to Quantify Error in Common Free Energy Methods. *J. Chem. Theory Comput.* **2011**, *7*, 4115−4134.
(52) Morais, A. R. C.; Harders, A. N.; Baca, K. R.; Olsen, G. M.; Befort, B. J.; Dowling, A. W.; Maginn, E. J.; Shiflett, M. B. Phase Equilibria, Diffusivities, and Equation of State Modeling of HFC-32 and HFC-125 in Imidazolium-Based Ionic Liquids for the Separation of R-410A. *Ind. Eng. Chem. Res.* **2020**, *59*, 18222−18235.
(53) Baca, K. R.; Olsen, G. M.; Matamoros Valenciano, L.; Bennett, M. G.; Haggard, D. M.; Befort, B. J.; Garciadiego, A.; Dowling, A. W.; Maginn, E. J.; Shiflett, M. B. Phase Equilibria and Diffusivities of HFC-32 and HFC-125 in Ionic Liquids for the Separation of R-410A. ACS Sustainable. *Chem. Eng.* **2022**, *10*, 816−830.
(54) Winn, J. S. The Fugacity of a Van Der Waals Gas. *J. Chem. Educ.* **1988**, *65*, 772.
(55) Sanmamed, Y.; González-Salgado, D.; Troncoso, J.; Romani, L.; Baylaucq, A.; Boned, C. Experimental Methodology for Precise Determination of Density of RTILs as a Function of Temperature and Pressure Using Vibrating Tube Densimeters. *J. Chem. Thermodyn.* **2010**, *42*, 553−563.
(56) He, M.; Peng, S.; Liu, X.; Pan, P.; He, Y. D. Diffusion Coefficients and Henry's Constants of Hydrofluorocarbons in [HMIM][Tf_2N], [HMIM][TfO], and [HMIM][BF_4]. *J. Chem. Thermodyn.* **2017**, *112*, 43−51.
(57) Dong, L.; Zheng, D.; Sun, G.; Wu, X. Vapor-liquid Equilibrium Measurements of Difluoromethane+[Emim] OTf, Difluoromethane +[Bmim] OTf, Difluoroethane+[Emim] OTf, and Difluoroethane +[Bmim] OTf Systems. *J. Chem. Eng. Data* **2011**, *56*, 3663−3668.
(58) Seddon, K. R.; Stark, A.; Torres, M.-J. Viscosity and Density of 1-Alkyl-3-methylimidazolium Ionic Liquids. *ACS Symp. Ser.* **2002**, *819*, 34−49.
(59) Ahosseini, A.; Scurto, A. M. Viscosity of Imidazolium-based Ionic Liquids at Elevated Pressures: Cation and Anion Effects. *Int. J. Thermophys.* **2008**, *29*, 1222−1243.
(60) Ciocirlan, O. Viscosities of 1-Hexyl-3-methylimidazolium Tetrafluoroborate and its Binary Mixtures with Dimethyl Sulfoxide and Acetonitrile. *J. Chem. Eng. Data* **2018**, *63*, 4205−4214.
(61) Mecklenfeld, A.; Raabe, G. Efficient Solvation Free Energy Simulations: Impact of Soft-core Potential and a New Adaptive λ-spacing Method. *Mol. Phys.* **2017**, *115*, 1322−1334.